Origin of intrinsic magnetic hardness in permanent magnets.

D. Haskel, [1] J. C. Lang, [1] Z. Islam, [1] A. Cady, [1] G. Srajer, [1] M. van Veenendaal,[1,2]

P. C. Canfield[3]

1. Advanced Photon Source, Argonne National Laboratory, Argonne, IL 60439, USA

2. Dept. of Physics, Northern Illinois University, De Kalb, IL 60115, USA

3. Dept. of Physics and Ames Laboratory, Iowa State University, Ames, IA 50011, USA

Abstract

Modern permanent magnets gain most of their intrinsic stability against demagnetizing fields through incorporation of rare-earth elements in their structure. This process, however, often results in the formation of complex crystal structures that typically place rare-earth atoms of the same type in inequivalent atomic environments, hindering a complete understanding of the rare-earth role. Using resonant diffraction of circularly polarized x rays we directly probed the magnetic moment reversal of each of the two inequivalent Nd rare-earth sites in a Neodymium-Iron-Boron magnet. The results show that the magnetic hardness of the current best permanent magnet has its atomic origins predominately at one of the two inequivalent Nd crystal sites.

Introduction

Magnetic hardness, a key property of permanent magnets, dictates the ability of a material to retain its magnetization after a magnetizing field is removed (remanence), or under the action of a demagnetizing field (coercivity). Developments in the synthesis of artificial, rare-earth (RE)-based permanent magnetic materials in the past two decades have yielded large increases in the remanent magnetic flux density compared to that of earlier steel and ferrite magnets (*1, 2*). This has enabled the miniaturization of permanent magnets and their subsequent widespread use in a variety of applications. While earlier quench-hardened steels gained significant magnetic hardness through the incorporation of defects and internal strain, modern magnets achieve much higher coercivities through the added intrinsic stability introduced with RE elements. Key to this progress is the fact that 4f electrons of RE elements, which can carry large orbital angular momentum in a partially filled 4f shell configuration, maintain their atomic character upon alloying with 3d transition metals (TM) (*3, 4*). The anisotropic charge distribution associated with a large orbital angular momentum state of 4f electrons interacts with the crystal electric field (CEF) of surrounding charges, favoring a preferred arrangement of the 4f charge density with respect to the crystalline axes. Since the spin-orbit interaction promotes collinearity of spin and orbital moments, a preferred orientation of the magnetic moment relative to the crystalline axis is established. The magneto-crystalline anisotropy (MCA) energy involved in disrupting this preferred orientational arrangement provides intrinsic stability against demagnetizing fields, resulting in the high coercivity of RE magnets. While the RE component provides most of the MCA responsible for the magnetic

hardness, the TM component provides most of the magnetization [e.g., ~$31\mu_B$ for Fe and ~$6\mu_B$ for Nd per formula unit in $Nd_2Fe_{14}B$ (5); μ_B is Bohr magneton.]
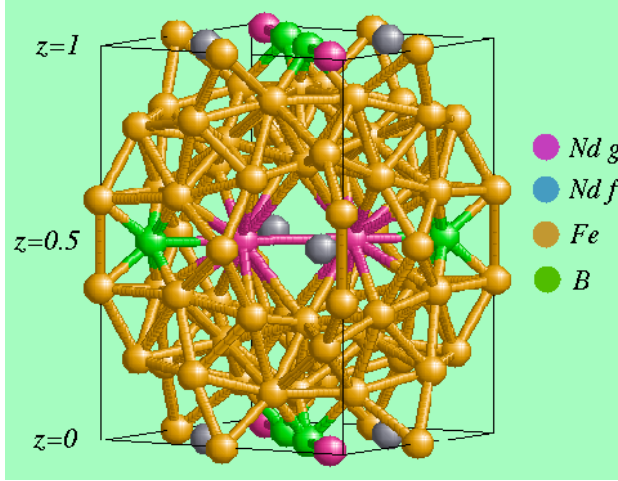

Figure 1: Unit cell of $Nd_2Fe_{14}B$. The unit cell contains four formula units (68 atoms). The two inequivalent Nd crystal sites that are the focus of this study are color coded (purple and blue). The six Fe inequivalent sites are not distinguished. Site notation is after Herbst *et al.* (20).

Despite great technological progress, our basic understanding of the atomic origins of MCA in these complex structures is limited. We focus here on $Nd_2Fe_{14}B$ since it is the best permanent magnetic material available today. As shown in Fig. 1, $Nd_2Fe_{14}B$ has a very large unit cell with two magnetic elements (Fe, Nd) each being present in more than one local atomic environment (i.e., inequivalent crystal sites having different coordination number or types of neighboring atoms, or a different point symmetry). While it is well established from studies of isostructural $(Gd,Y)_2Fe_{14}B$ crystals that Fe contributions to MCA in $Nd_2Fe_{14}B$ favor a [001] easy-axis alignment of the magnetization (6, 7) (Y is non-magnetic and Gd has zero orbital angular momentum and does not contribute to MCA), Nd contributions to MCA are larger by at least a factor of 3-4 at ambient and low temperatures (5). Despite Nd dominating the MCA, the relative importance of each of the two inequivalent Nd lattice sites in regulating the magnetic

hardness of $Nd_2Fe_{14}B$ has not yet been determined in a measurement. The determination of non-collinear Nd moments from neutron diffraction measurements is a challenge as only two of the sixteen magnetic atoms per formula unit are rare earths, and the magnetic contribution is only a fraction of the total neutron scattered intensity (*5, 8*). Another probe of magnetism is x-ray magnetic circular dichroism (XMCD), which has the advantage of separating magnetic contributions by element type (*9-11*). Such measurements were very valuable in probing the minority Nd sublattice outside the overwhelming magnetic background of the majority Fe sublattice. For example, they showed that the average Nd atom undergoes a much larger spin-reorientation than the average Fe atom below T~130 K, resulting in a complex non-collinear magnetic structure yet to be explained by theory [*12,13*]. XMCD, however, an absorption technique, cannot separate the magnetic contributions of Nd (or Fe) atoms in inequivalent lattice sites since small chemical shifts of site-specific absorption thresholds result in overlapping absorption spectra.

As shown below, a new experimental x-ray scattering approach allows separation of the contributions of the inequivalent Nd crystal sites to magnetic hardness. The measurements show that whereas one set of Nd sites strongly favors magnetic alignment along the [001] direction dominating the intrinsic MCA of $Nd_2Fe_{14}B$, the other set in fact reduces the intrinsic stability by favoring the *xy*-plane. Our conclusions have strong implications for the understanding of magnetic hardness in this class of materials.

Measurements and results

Site separation is achieved by exploiting the symmetry properties of the crystal's space group, which determine the relative scattering contributions of inequivalent crystal sites to the intensity of symmetry-allowed Bragg reflections. Element-specificity is obtained by tuning the x-ray energy to near the Nd L_2 resonance ($2p_{1/2} \rightarrow 5d$ dipole transition at 6.722 keV), and resonant diffraction of circularly polarized x-rays is used to yield magnetic sensitivity ([14, 15]). The latter arises because the excited spin-polarized electron is sensitive to the exchange splitting of Nd $5d$ resonant states, which is proportional to the Nd 4f magnetic moment ([16-18]). A differential measurement of the resonantly scattered intensity for opposite x-ray helicities ($I^+ - I^-$) yields elemental magnetic sensitivity while the sum, ($I^+ + I^-$), yields chemical sensitivity ([19]). A flipping ratio is defined as ($I^+ - I^-$)/($I^+ + I^-$).

Figure 2(a-c) shows room temperature resonant charge and magnetic-sensitive dichroic scattered intensities for (110), (220), and (440) Bragg reflections. These reflections probe Nd g sites, Nd f sites, and both sites equally, respectively (Table I). The dichroic scattering at (110) and (220) reflections probes Nd magnetism in an element- and site-specific way. There are no magnetic contributions from Fe, since the resonant magnetic scattering amplitude f_m is practically zero away from element-specific resonances, as shown in Fig. 2d ([19]).
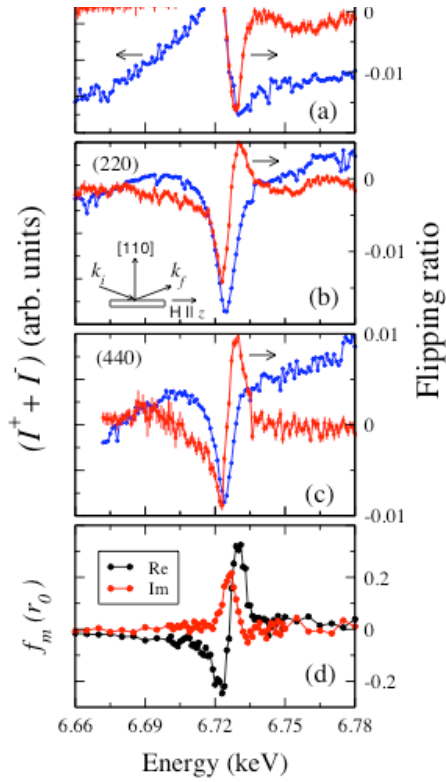
Figure 2. Magnetic-sensitive resonant diffraction. Resonant diffraction scans through the Nd L_2 absorption edge for selected Bragg reflections (a-c). Blue curves correspond to resonant charge scattering and red curves are magnetic-sensitive scattering. An H=6.0 kOe field is applied along the [001] easy axis direction, which is contained in the scattering plane, and saturates the sample magnetization. The inset in (b) shows the scattering reflection geometry with k_i and k_f incident and scattered wavevectors. Panel (d) shows the site-averaged Nd magnetic resonant scattering amplitude obtained from XMCD measurements and related Kramers-Krönig transform (*23*).

Element- and site-specific Nd spin reversal curves were then measured through changes in the magnetic-sensitive dichroic scattering as an applied field was looped while maintaining the selected diffraction condition at a fixed resonant energy that maximizes magnetic contrast. These loops are shown in Figure 3, which includes reversal curves for inequivalent Nd *f* and *g* sites (Fig. 3a), together with site-averaged Nd reversal loops independently determined from (440) dichroic scattering, XMCD, and by equally weighting site-specific (110) and (220) dichroic scattering loops (Fig. 3b).
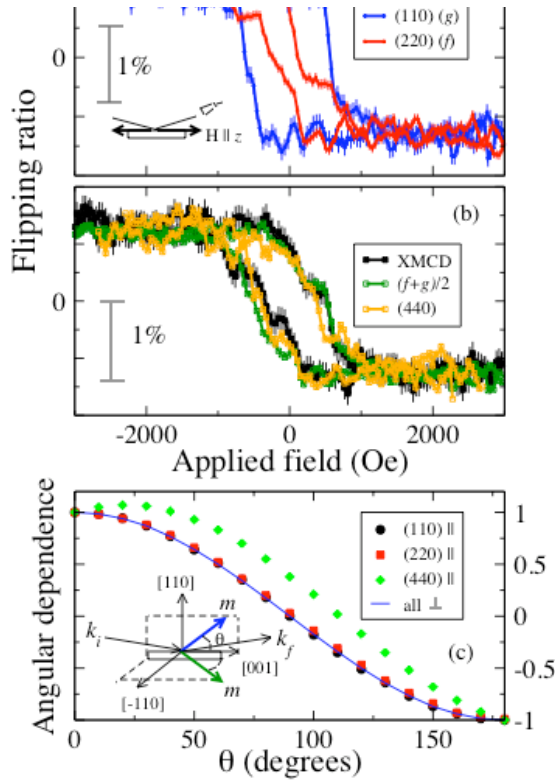
Figure 3: Site-specific Nd spin reversal curves. (a) Site-selective Nd spin-reversal loops measured through magnetic-sensitive dichroic resonant scattering at (110) and (220) Bragg reflections. (b) Site-averaged loops, obtained from XMCD measurements, (440) dichroic resonant scattering, and by averaging the curves in panel (a). Loops are normalized to match at saturation. The XMCD loop was multiplied by -1 (see Fig. S1). The angular dependence of dichroic resonant scattering (*19*) for spin rotation parallel (∥) or perpendicular (⊥) to the scattering plane is shown in (c); θ is the angle with the *z*-axis. The perpendicular case gives a pure cosθ dependence for all Bragg reflections. Values are normalized to those of $\hat{m}$∥[001].

Different reversal loops for (110), (220), and (440) diffraction conditions can only result from a coherent reversal process. Macroscopic domain nucleation and growth would have resulted in equal loops (normalized to saturation value) for (110) and (220) reflections due to incoherent superposition of scattering from oppositely oriented magnetic domains. This is because the angular dependence of dichroic resonant scattering, which depends on the relative orientation of x-ray scattering vectors and magnetic moment direction (*19*), is

nearly the same for (110) and (220) reflections when normalized to its value for $\hat{m} \parallel [001]$ (Fig. 3c). It follows that the response of Nd magnetic moments to a reversed applied field depends on the Nd crystal site. The Nd g site exhibits an ideal easy-axis loop with high coercive squareness or hardness while the Nd f site shows magnetically soft behavior. Since [001] is the macroscopic magnetic easy-axis, and, since Nd dominates the MCA in this material, this result alone indicates that Nd g sites are predominately responsible for the intrinsic magnetic hardness of $Nd_2Fe_{14}B$.

We note that kinematically diffracted x-rays penetrate deeper into the sample at (220) than (110) Bragg reflections ($\approx 2\mu m$ versus $1\mu m$, respectively). However, we can rule out near-surface decomposition or impurity phases being responsible for the measured differences based on (a) identical normalized fluorescence XMCD loops at (110) and (220) incident Bragg angles (Fig. S1), and (b) clean and sharp single-crystal diffraction peaks corresponding to the nominal crystal structure of $Nd_2Fe_{14}B$. An intrinsic advantage of this method is that magnetization is probed using selected Bragg diffraction conditions, so phase-specificity is inherent in addition to element- and site-selectivity.

Discussion

Changes in dichroic resonant scattering with applied field come from its angular dependence, $[(\hat{k}_i \cdot \hat{m}) + (\hat{k}_f \cdot \hat{m})\cos 2\theta]$, with $\hat{k}_i$ and $\hat{k}_f$ incident and scattered wave vectors, respectively, $\hat{m}$ the magnetic moment direction, and θ the Bragg angle (20). As the moments rotate, their orientation with respect to the x-ray scattering vectors changes while their magnitude does not. This angular dependence results in sign reversal upon

magnetization reversal and sensitivity to the magnetization component in the scattering plane only (Fig. S2). This sensitivity to moment orientation, coupled to site-selectivity through choice of diffraction condition, makes this dichroic signal a unique tool for studies of magnetization reversal in crystals with inequivalent sites. For low Bragg angle (110) and (220) reflections, the angular dependence results in a near $\cos\theta$ dependence, whether the moments rotate in the scattering plane or perpendicular to it (θ is the angle with the z-axis, see Fig. 3c) [at low Bragg angles the angular dependence can be approximated as $\approx (\hat{k}_i + \hat{k}_f) \cdot \hat{m} = m_z$]. In this respect, the dichroic scattering loops for (110) and (220) reflections, normalized to saturation, can be regarded as conventional loops that measure the projection of site-specific moments into the z-axis.

The reversal loops shown in Fig. 3 clearly indicate a preference for the g sites to align with the crystal's z-axis. The high squareness of this site-specific loop indicates magnetically hard behavior, where a reversed applied field of H=-600 Oe is needed to cause spin reversal. The reversal to the $-z$ direction is sharp, since the spins avoid other crystal orientations. The f sites, however, start reversing at very low fields and in fact display magnetically soft behavior for H‖[001]. Clearly the Fe-Nd exchange field forces the spins at f sites to align with the [001] direction at saturation, but their interaction with the CEF does not favor z-axis alignment, as verified by theoretical calculations detailed below.

The angular dependence of dichroic resonant scattering reveals a non-trivial reversal process due to competing anisotropies at inequivalent Nd sites. Since the dichroic

scattering signal at (110) and (220) reflections almost vanishes for $\hat{m}\perp[001]$ (either in the scattering plane or perpendicular to it) (Fig. 3c), a nearly orthogonal arrangement of magnetic moments at Nd f and g sites occurs at a reversed applied field H=-200 Oe. At this field value the g moments remain along the z direction (due to their stronger coupling to the lattice) while the f moments lie in the plane perpendicular to it. This unusual reversal must be accompanied by an inhomogeneous arrangement of Fe moments, as they couple through Fe-Nd and Fe-Fe direct exchange [Nd-Nd coupling is indirect, and weak (13)]. It is likely that the exchange price of such an inhomogeneous Fe/Nd configuration limits the extent of f moment rotation past the xy-plane, introducing a "plateau" in the (220) loops until the delayed reversal of g moments takes place. We note that a complete microscopic picture cannot be obtained from this data alone, since probing the atomic details of Fe reversal with this technique is complicated by the presence of six inequivalent Fe crystal sites (20).

Our experimental findings are supported by theoretical calculations of the MCA energies governing the spin reversal. We have performed numerical and analytical calculations of the dependence of the energy on the direction of the magnetic moment at Nd sites. The results of both approaches are in good agreement and are presented in Fig. 4. Numerical calculations were done for a Nd^{3+} ion, including the full Coulomb multiplet interaction and the 4f spin-orbit coupling. Direct and exchange Coulomb parameters were obtained in the Hartree-Fock limit and scaled down to 80% to account for screening effects (21). The crystal-field interaction is expanded in terms of spherical tensor operators, $H_{CF} = \sum_i B_{kq}\left(C_q^k\right)_i$, where B_{kq} are crystal field parameters and the summation is over the

electrons of the rare-earth ion. We include terms up to fourth order as higher order terms are important only at lower temperatures (*13,22*). While the CEF acting on each Nd ion has orthorhombic (*mm*) point symmetry, a screw axis in the tetragonal $P4_2/mnm$ space group causes a sign change of the $B_{n,-2}(n=2,4)$ for equivalent sites in $z=0$ and $z=1/2$ planes (see Fig. 1), subdividing the sites magnetically into $f_{1,2}$ and $g_{1,2}$. CEF parameters are taken from Yamada *et al*. (*13*). Figure 4 shows the change in anisotropy energy for the *f* and *g* Nd sites as a function of the angle θ between the magnetic moment and the [001] axis. The moments are forced to an angle of $\varphi=45°$ with the [100] axis. The red squares in Fig. 4 show that the MCA energy of g sites strongly increases as these moments are forced away from the *z*- axis towards the *xy*-plane ($\theta=90°$). This is always the case, independent of the in-plane angle φ (Fig. S3), clearly showing that the *g* sites strongly favor a [001] orientation. However, the *f* sites favor the *xy*-plane, as their MCA energy is minimized at $\theta=90°$. Analytical calculations of the in-plane MCA energy shows that f_1 and f_2 sites prefer [-110] and [110] orientations, respectively (Fig. S3).
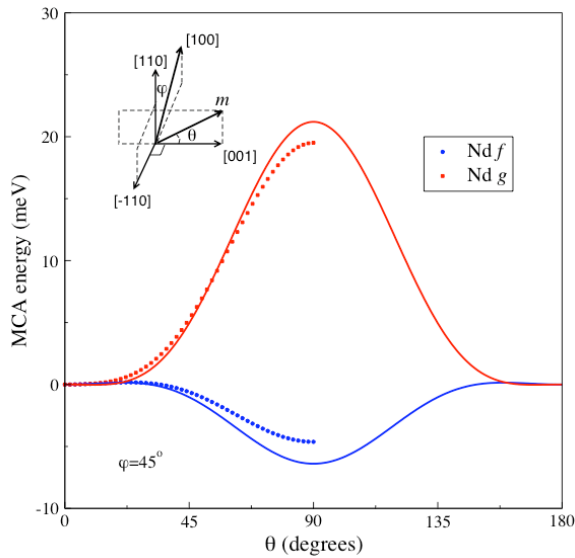

Figure 4. Calculated anisotropy energy. The anisotropy energy as a function of the angle θ between the magnetic moment and the *z*-axis. φ is in the xy-plane, away from the [100] direction. Points and lines correspond to numerical and analytical calculations, respectively.

11

An alternative, analytical approach is to approximate the angular dependence of the anisotropy energy by taking the expectation value of the CEF in the lowest Hund's rule multiplet $\langle LSJ, M = -J \,|\, H_{CF} \,|\, LSJ, M = -J \rangle$, thereby assuming a strong molecular field along the z-axis. Evaluation using the Racah method gives an anisotropy energy of $E_{an}=$ ($K_1 \sin^2\theta + K_2 \sin^4\theta$), where $\varphi=45°$ is assumed and K_1 and K_2 can be obtained from the crystal field parameters B_{kq} (*13*). For the f_2 site in the [110] direction (and the f_1 site in the [$\bar{1}$10] direction) the parameters are K_1=2.30 and K_2=-8.69 meV. From the solid curves in Fig. 4 we clearly see a decrease in energy when rotating the spin, indicating that the f sites prefer to lie in the xy-plane. For the $g_{1,2}$ sites, $K_1+K_2 > 0$ for all values of φ, and the magnetic moment prefers to lie along the z-axis. This clearly strengthens the site-selective z-axis reversal data obtained with dichroic resonant scattering of high coercive squareness for g sites and soft magnetic behavior for f sites.

Conclusions

We provide experimental and theoretical evidence that the magnetic hardness of currently best permanent magnetic material $Nd_2Fe_{14}B$ arises predominately from one of the two

inequivalent Nd sites. While one Nd site (*g*) strongly prefers the [001] direction at ambient temperature and dictates the macroscopic easy axis direction, the other Nd site (*f*) (containing half of all the Nd atoms) reduces the intrinsic stability by favoring alignment along [110]-type directions. Since the local atomic environments of these inequivalent Nd sites are known (*20*), it may be possible that future permanent magnetic materials will make more efficient use of all the RE atoms, rather than half of them, to yield further enhancements of magnetic hardness. Clearly these developments rely on a detailed understanding of the atomic origins of magneto-crystalline anisotropy in these materials. As demonstrated here, progress in this direction can be achieved by the combination of site-specific diffraction with the spectroscopic, elemental magnetic fingerprints obtained near atomic resonances. The manipulation of structures at the atomic level enabled by recent advances in nanotechnology could provide a venue to achieve further enhancements in magnetic hardness by tailoring the local atomic structure.

References

1. K. H. J. Buschow, in *Ferromagnetic Materials*, E. P. Wohlfarth, K. H. Buschow, Eds. (North-Holland, Amsterdam, 1988).

2. J. M. D. Coey, J. M. Cadogan, D. H. Ryan, in *Nd-Fe Permanent Magnets: their present and future applications*, I. V. Mitchell, Ed. (Elsevier Applied Science, London/New York, 1985), p. 143.

3. K. Hummler, M. Fähnle, *Phys. Rev. B* **45**, 3161 (1992).

4. D. J. Sellmyer, M. A. Engelhardt, S. S. Jaswal, A. J. Arko, Phys. Rev. Lett. **60**, 2077 (1988).

5. J. F. Herbst, *Reviews of Modern Physics* **63**, 819 (1991).

6. D. Givord, H. S. Li, R. Perrier de la Bâthie, *Solid State Communications* **51**, 857 (1984).

7. M. Bogé *et al.*, *Solid State Communications* **55**, 295 (1985).

8. P. Wolfers, S. Obbade, D. Fruchart, R. Verhoef, *J. of Alloys and Compounds* **242**, 74 (1996).

9. G. Schütz *et al.*, *Phys. Rev. Lett.* **58**, 737 (1987).

10. J. Stöhr, *J. Magn. Magn. Mater.* **200**, 470 (1999).

11. P. Carra, M. Altarelli, *Phys. Rev. Lett.* **64**, 1286 (1990).

12. J. Chaboy *et al.*, *Phys. Rev. B* **57**, 8424 (1998).

13. M. Yamada, H. Kato, H. Yamamoto, Y. Nakagawa, *Phys. Rev. B* **38**, 620 (1988).

14. S. W. Lovesey, S. P. Collins, in *X-ray Scattering and Absorption by Magnetic Materials* (Clarendon Press, Oxford, 1996).

15. H. A. Durr *et al.*, *Science* **284**, 2166 (1999).

16. J. P. Hannon, G. T. Trammell, M. Blume, D. Gibbs, *Phys. Rev. Lett.* **61**, 1245 (1988).

17. J. Miguel-Soriano, J. Chaboy, L. M. Garcia, F. Bartolomé, H. Maruyama, *J. Appl. Phys.* **87**, 5884 (2000).

18. P. Carra, M. Altarelli, F. de Bergevin, *Phys. Rev. B* **40**, 7324 (1989).

19. Materials and methods are available as supporting material on *Science* Online.

20. J. F. Herbst, J. J. Croat, F. E. Pinkerton, W. B. Yelon, *Phys. Rev. B* **29**, 4176 (1984).

21. R. D. Cowan, in *Theory of Atomic Structure and Spectra* (Univ. of California Press, Berkeley, 1981).

22. J. M. Cadogan, J. M. D. Coey, J. P. Gavigan, D. Givord, H. S. Li, *J. Appl. Phys.* **61**, 3974 (1987).

23. The optical theorem results in $XMCD \propto Im(f_m)$. We used tabulated bare-atom scattering factors away from resonance for absolute normalization and a Kramers-Krönig transformation to obtain Re (f_m).

Supporting Online Material

Materials and methods

Figs. S1, S2, S3

Table I. Site-specific contributions to Bragg diffraction. Relative percentage contributions of inequivalent Nd sites to the scattering amplitude of selected Bragg reflections with scattering **Q** vectors along [110]. Ratios are obtained from site-specific structure factors $\sum_{n=1}^{4} e^{i\vec{Q} \cdot \vec{r}_n}$, where the sum is over the four *equivalent* Nd sites in the unit cell (*f* or *g* Wyckoff sites), and r_i are their atomic positions.

Site	(110)	(220)	(440)
Nd *f*	3	96.4	48.5
Nd *g*	97	3.6	51.5

Supporting Online Material

Materials and methods

(i) *Experimental details*

Measurements were done at undulator beamline 4-ID-D of the Advanced Photon Source on a $Nd_2Fe_{14}B$ single crystal grown out of a Nd-rich ternary melt (*1,2*). The [110] surface of the crystal was oriented along the scattering vector. An electromagnet delivered a magnetic field (± 6 kOe) along the [001] easy axis direction, which was parallel to the sample surface and in the scattering plane. A PZT-driven diamond (111) phase-retarder operated in Bragg transmission geometry (*3*) was used to convert the x-ray polarization from linear to circular and to rapidly (1 Hz) switch between opposite x-ray helicities. The dichroic diffraction was measured through the Nd L_2 resonance using a digital lock-in detection scheme that synchronizes the measured x-ray diffracted intensity with the helicity modulation of the incoming x-ray beam (*4*). The Si(111) double-crystal monochromator, phase-retarder, and sample's Bragg angles were tracked to maintain their respective diffraction conditions through the resonance energy scans. XMCD measurements were performed concomitantly by measuring the Nd L_β fluorescence for opposite x-ray helicities using energy-dispersive Si-drift diode detectors. All measurements were done at ambient temperature.

(ii) *Dichroic resonant scattering of circularly polarized x-rays*

A differential measurement of resonantly diffracted intensities for opposite x-ray helicities removes pure charge resonant scattering and yields charge-magnetic interference scattering, which contains information on both magnitude and direction of the resonant atom's magnetic moment. Following Hannon *et al*. (*5*), the resonant scattering amplitude from a single magnetic ion is given by $f = f_e(Q,E)(\hat{\varepsilon}'^* \cdot \hat{\varepsilon}) - if_m(E)(\hat{\varepsilon}'^* \times \hat{\varepsilon}) \cdot \hat{m}$, with f_e and f_m complex charge and magnetic-sensitive scattering amplitudes, respectively. $\hat{\varepsilon}$ and $\hat{\varepsilon}'$ are incident and scattered polarization vectors, respectively, and $\hat{m}$ is the magnetic moment direction. The scattered intensity from a crystal of magnetic ions is given by the modulus square of the structure factor $|F(Q,E)|^2 = \left| \sum_n f_n e^{i\vec{Q}\cdot\vec{r}_n} \right|^2$, where the sum is over all atoms in the unit cell and thermal disorder is neglected. Since reversing x-ray helicity is equivalent to reversing magnetization direction, a differential measurement of diffracted intensity for opposite x-ray helicities $(I^+ - I^-)$ removes pure charge terms ($f_e^* f_e$, independent of $\hat{m}$) and pure magnetic-sensitive terms ($f_m^* f_m$, quadratic in $\hat{m}$), and includes contributions from charge-magnetic interference (CMI) terms only (i.e., $-i \sum_{i,j} A^* B_j f_{e,i}^* f_{m,j} e^{i\vec{Q}\cdot(\vec{r}_i - \vec{r}_j)} + c.c.$), proportional to $\hat{m}$ (A and B are polarization factors). Information on the magnitude of the resonant atom's magnetic moment is contained in f_m, and information on its direction relative to the x-ray polarization vectors is in $B = (\hat{\varepsilon}'^* \times \hat{\varepsilon}) \cdot \hat{m}$. Adding diffracted intensities for opposite x-ray helicities removes CMI scattering and practically measures resonant charge scattering since $f_m^2 << f_e^2$.

An explicit derivation of the angular dependence of dichroic CMI scattering (A^*B) for our scattering geometry can be obtained from the density matrix formalism of Blume and Gibbs (6) for the case of no polarization analysis of the outgoing beam. This involves taking traces over matrix products of the form $\langle \hat{\varepsilon}'^* \cdot \hat{\varepsilon} \rangle \rho \langle [(\hat{\varepsilon}'^* \times \hat{\varepsilon}) \cdot \hat{m}] \rangle^\dagger$, where ρ is the density matrix of a circularly polarized beam, and $\langle \; \rangle$ indicates matrix representation using the (σ, π) basis (σ and π are polarization components perpendicular and parallel to the scattering plane, respectively). In this representation these matrices are (6, 7):

$$\rho_{L,R} = \begin{pmatrix} 1 & \mp iP_c \\ \pm iP_c & 1 \end{pmatrix}$$

$$\langle \hat{\varepsilon}'^* \cdot \hat{\varepsilon} \rangle = \begin{pmatrix} 1 & 0 \\ 0 & \hat{k}' \cdot \hat{k} \end{pmatrix} \qquad .$$

$$\langle (\hat{\varepsilon}'^* \times \hat{\varepsilon}) \cdot \hat{m} \rangle = \begin{pmatrix} 0 & -\hat{k}' \cdot \hat{m} \\ \hat{k} \cdot \hat{m} & (\hat{k}' \times \hat{k}) \cdot \hat{m} \end{pmatrix}$$

Here P_c is the degree of circular polarization. While $\pi \rightarrow \pi'$ scattering probes the component of magnetization perpendicular to the scattering plane ($(\hat{k}' \times \hat{k}) \cdot \hat{m}$ term), its contribution to the trace of the matrix product is helicity independent and cancels in the differential measurement of dichroic CMI scattering. This formalism yields $[(\hat{k}_i \cdot \hat{m}) + (\hat{k}_f \cdot \hat{m}) \cos 2\theta]$, with $\hat{k}_i$ and $\hat{k}_f$ incident and scattered wave vectors, respectively, and θ the Bragg angle.

References

1. P. C. Canfield, Z. Fisk, *Phil. Mag. B* **65**, 1117 (1992).

2. P. C. Canfield, I. R. Fisher, *J. Crystal Growth* **225**, 155 (2001).

3. K. Hirano, K. Izumi, T. Ishikawa, S. Annaka, S. Kikuta, *Jpn. J. Appl. Phys*. **30**, L407 (1991).

4. Y. Hayasaki *et al*., *J. Phys.: Condens. Matt*. **16**, 1915 (2004).

5. J. P. Hannon, G. T. Trammell, M. Blume, D. Gibbs, *Phys. Rev. Lett*. **61**, 1245 (1988).

6. M. Blume, D. Gibbs, *Phys. Rev. B* **37**, 1779 (1988).

7. J. P. Hill, D. F. McMorrow, *Acta Cryst*. **A52**, 236 (1996).
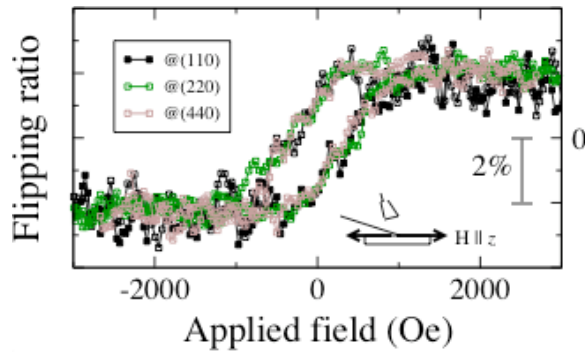
Supporting online figures

Figure S1. XMCD reversal loops measured in fluorescence geometry. The incident angles are 8.51°, 17.25°, and 36.34° for (110), (220), and (440) Bragg reflections at incident x-ray energies of 6.730, 6.724, and 6.725 keV, respectively. These energies maximize the dichroic scattering signals (Fig. 2), which are measured concomitantly (Fig. 3). Loops are normalized to saturation values. The opposite sign of XMCD loops relative to those measured in dichroic scattering (Fig. 3) is due to opposite signs of real and imaginary parts of f_m at selected x-ray energies and to the interference between chemical and magnetic resonant contributions (*19*), which modulates the sign of dichroic scattering differently for different **Q** vectors (structure factor effects).
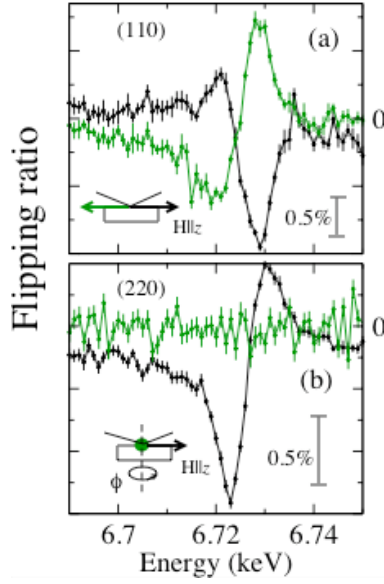
Figure S2. Angular dependence of dichroic scattering. The cross section results in sign reversal upon reversal of the magnetization direction (a) and sensitivity to magnetization component in the scattering plane only (b). In (b) the sample/magnet assembly was rotated so that the applied field remains along z but is perpendicular to the scattering plane.
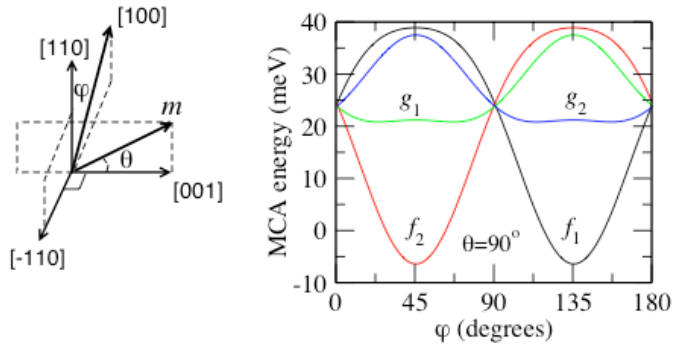

Figure S3. Anisotropy energy for moment alignment in the xy-plane. Curves are results from analytical calculations. The g sites prefer to align with the z-axis, as forcing them into the xy-plane raises their MCA energy by at least 20 meV. The f_1 and f_2 sites, however, prefer [-110] and [110] alignment in the xy-plane, respectively, where their MCA energy is lowest (the screw axis in the structure causes f_1 and f_2 sites to prefer orthogonal axis).